

Angular width of a narrow beam for X-ray linear attenuation coefficient measurements

S. Midgley

Monash Centre for Synchrotron Science, School of Physics, Monash University, VIC 3800, Australia

Received 6 December 2005; accepted 24 January 2006

Abstract

The detection of scattered radiation can be a major source of systematic errors when measuring the X-ray linear attenuation coefficient, μ . Angular distributions of scattered photons are studied for $Z = 1$ to 20 at energies 6 keV to 100 MeV, using tabulated atomic form factors and incoherent scattering functions. A circularly symmetric pencil beam irradiation geometry is considered, and scatter acceptance angles, equal to the sum of the incident and exit beam divergence, are evaluated for systematic errors of 0.5–1.0% in measuring μ . The analysis is extended to water, comparing predictions based upon the independent atomic model to values obtained from tabulated molecular form factors.

© 2006 Elsevier Ltd. All rights reserved.

1. Introduction

The key items of equipment for measuring the X-ray linear attenuation coefficient μ are; a “narrow” beam of mono-energetic X-rays, the sample, detector and collimation (see Fig. 1). The relationship between the incident and transmitted beam intensities, I_o and I_t , is given by the exponential attenuation law (see e.g., Perrin, 1948), which is written

$$\sum_L \mu t = -\ln\left(\frac{I_t}{I_o}\right). \quad (1)$$

In this expression, the left-hand side is known as the ray-sum and represents the product of attenuation coefficients and thickness t for volume elements along the ray path, L . For a homogeneous sample, the X-ray linear attenuation coefficient is obtained simply by dividing by the measured thickness.

The principal sources of systematic errors in evaluating Eq. (1) are; beam hardening due to the finite spread of photon energies in the transmitted beam, and the detection of forward scattered radiation. These can be minimised by ensuring that the recorded intensity is almost mono-energetic, and by placing collimators around the sample to minimise the production and detection of scattered radiation (Creagh and Hubbell, 1987, 1990). In practice, there is a trade off between meeting these two requirements and maintaining sufficient beam intensity to complete the measurement in a reasonable amount of time.

The question as to what is an acceptable amount of scattered radiation reaching the detector, has been addressed for mega voltage energies by Davisson and Evans (1952) and Barrett and Swindell (1981). In this energy regime, only incoherent scattering needs to be considered, and can be treated as a Compton process which is independent of the sample composition. The author is not aware that this question has been answered for diagnostic X-ray energies (approximately

E-mail address: stewart.midgley@sync.monash.edu.au.

15–150 keV), where coherent scattering is also of some importance, producing an angular distribution that is peaked in the forward direction (Morin and Berroir, 1983; Johns and Yaffe, 1983). We examine the influence of scattered radiation on μ measurements for both processes, at photon energies 6 keV to 100 MeV, and for low atomic number elements $1 \leq Z \leq 20$. The aim of this study is to determine the maximum angular width for a “narrow” beam.

2. Materials and methods

The irradiation geometry, illustrated in Fig. 1, places both entry and exit collimators around the sample to produce a circularly symmetric pencil beam of radiation. The “narrowness” of the beam is characterised by the scatter acceptance angle, θ_{sc} which is the sum of the incident beam divergence θ_{in} and the angle θ_{out} , subtended by the exit collimation (Davisson and Evans,

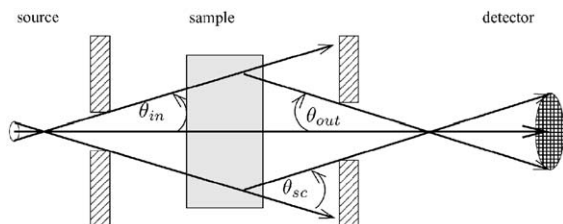


Fig. 1. Schematic representation of X-ray transmission measurement apparatus.

1952). The detector records forward scattered photons, with intensities I_{coh} and I_{inc} due to coherent and incoherent scattering interactions. Introducing the scatter to primary ratio SPR,

$$SPR = \frac{I_{coh} + I_{inc}}{I_t}, \quad (2)$$

the right hand side of Eq. (1) becomes,

$$-\ln\left(\frac{I_t + I_{coh} + I_{inc}}{I_o}\right) = \mu t - \ln(1 + SPR), \quad (3)$$

where the logarithmic term is the systematic error due to the detection of scattered radiation.

The production of forward scattered radiation is a function of the energy, composition and angular dependence of the respective differential scattering cross-sections (representing the probability for a deflection into a solid angle $d\Omega$). The relative importance of each scattering process is illustrated in Fig. 2, which was evaluated from the Lawrence Livermore National Laboratory (LLNL) tabulation (Cullen et al., 1989; Boone and Chavez, 1996). Coherent scattering is only of significance for lower atomic number (Z) elements at lower photon energies. Incoherent scattering is the dominant interaction process for diagnostic X-ray energies and up to several MeV (see Fig. 2(b)).

The angular distributions of scattered photons are examined in Sections 2.1 and 2.2, and the methodology for quantifying the systematic error in Eq. (3) are described in Sections 2.3 and 2.4.

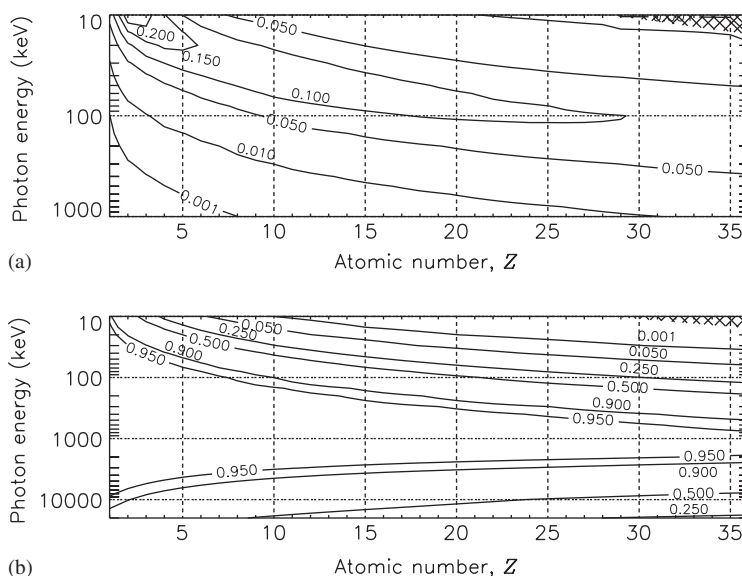


Fig. 2. Fractional contribution to the total X-ray interaction cross-section from (a) coherent and (b) incoherent scattering, where the region below the K-edge is shaded.

2.1. Scattering by atomic electrons

For un-polarised radiation, the differential cross-section for coherent scattering is given as,

$$\frac{d\sigma_{\text{coh}}}{d\Omega} = \frac{d\sigma_{\text{Th}}}{d\Omega} |F(x, Z)|^2, \quad (4)$$

where $d\sigma_{\text{Th}}/d\Omega$ is the Thomson cross section and $F(x, Z)$ is the atomic form factor. For incoherent scattering,

$$\frac{d\sigma_{\text{inc}}}{d\Omega} = \frac{d\sigma_{\text{KN}}}{d\Omega} S(x, Z), \quad (5)$$

where $d\sigma_{\text{KN}}/d\Omega$ is the differential Klein–Nishina cross section (for un-polarised radiation) and $S(x, Z)$ is the incoherent scattering function. For radiation with wavelength λ and deflection through θ , the momentum transfer parameter is $x = (1/\lambda) \sin(\theta/2)$. Atomic form factors $F(x, Z)$, and incoherent scattering functions $S(x, Z)$ are obtained from quantum mechanical radial probability density functions (see e.g., Hubbell and Øverbø, 1979).

The angular distribution of coherent scattered photons is illustrated in Fig. 3. Small values of x represent small deflections (or low photon energies) where $F(x, Z)$ approaches Z , whilst at large x values $F(x, Z)$ tends towards zero. Hence, the coherent scattering distribution is confined to the forward

direction with an angular extent that becomes narrower at higher photon energies and for decreasing Z .

For incoherent scattering by free and stationary electrons, $S(x, Z)$ is unity. At low energies, this produces an angular distribution that is symmetrically distributed between forward and back scattering with a minima at 90° , and becomes forward peaked at higher energies (see e.g., Barrett and Swindell, 1981). For incoherent scattering by bound atomic electrons, $S(x, Z)$ approaches zero for small x and tends towards Z for larger values (see Hubbell et al., 1975). This leads to the suppression of incoherent scattering in the forward direction as illustrated in Fig. 4, otherwise the angular distribution has the same general features as for scattering by free and stationary electrons.

2.2. Scattering by molecules

Small angle X-ray scattering (SAXS) arises from coherent scattering by atomic electrons within molecules. As the X-rays pass through the sample, the electrons resonate at the applied frequency and emit coherent secondary radiation, which then interferes. The key features of the interference pattern are the suppression of scattering in the forward direction (free atom behaviour was presented in Fig. 3) resulting in the presence of one or more diffraction peaks at small angles

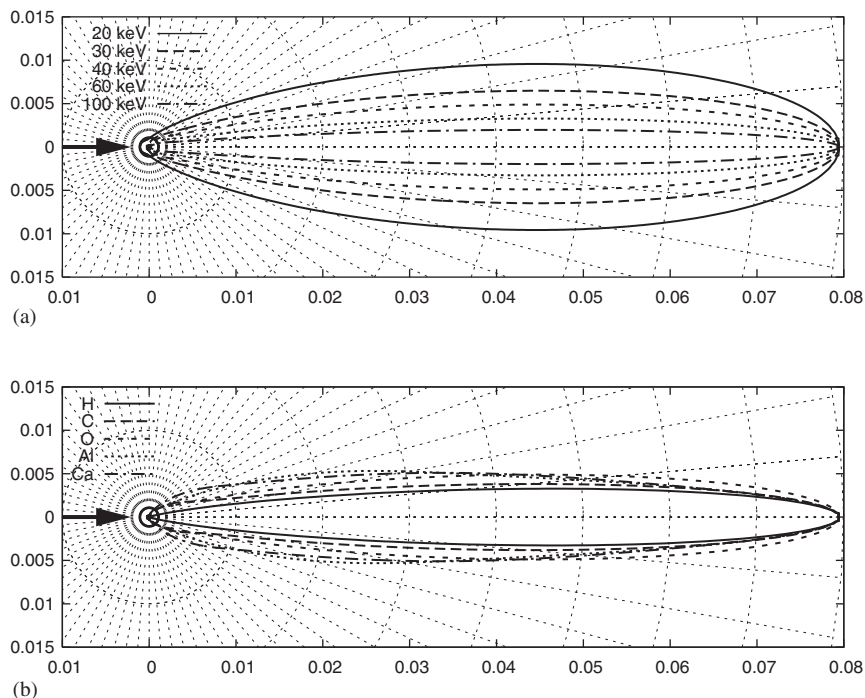


Fig. 3. Polar representation of coherent differential scattering cross-sections (barn/electron) for (a) oxygen as a function of energy and (b) for selected elements at 40 keV.

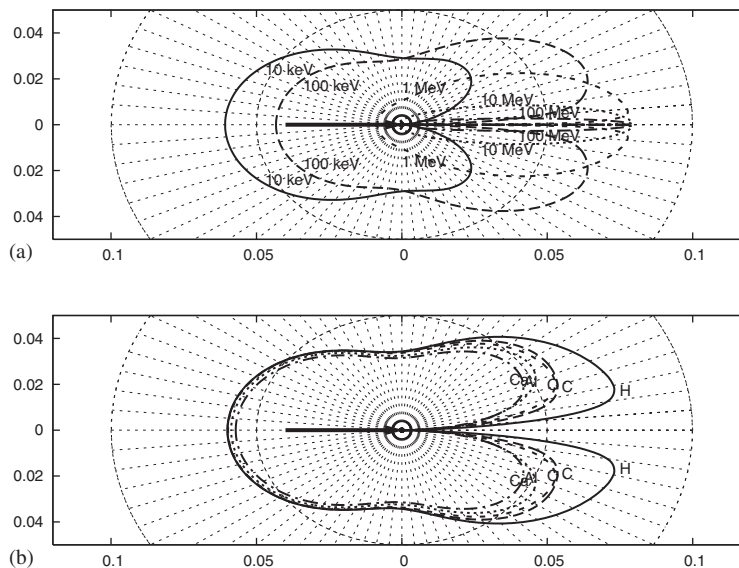


Fig. 4. Polar representation of incoherent differential scattering cross-sections (barn/electron) (a) oxygen as a function of energy and (b) $Z = 1-20$ at 40 keV.

(Kozanetzky et al., 1987; Harding and Schreiber, 1999). The diffracting structures often have relatively large dimensions (i.e., exceeding atomic spacing), so the diffraction peaks are located at very small angles. This is described using the same formalism used for coherent scattering, whereby molecular form factors are introduced into Eq. (4), i.e.,

$$\frac{d\sigma_{\text{coh}}}{d\Omega} = \frac{d\sigma_{\text{Th}}}{d\Omega} |F_{\text{mol.}}(x)|^2. \quad (6)$$

Molecular scattering can be divided into three distinct regimes according to the momentum transfer parameter x . It is technically difficult to separate very small deflections from the transmitted beam, and the region $x \leq 0.05 \text{ \AA}^{-1}$, is termed low angle X-ray scatter (LAXS). For low x values, $0.05 \text{ \AA}^{-1} \leq x \leq 0.50 \text{ \AA}^{-1}$, the diffraction pattern contains one or more peak-like structures, and is known as the region of small angle X-ray scatter (SAXS). For larger x values (i.e., $x \geq 0.5 \text{ \AA}^{-1}$) the atomic scattering centres exhibit free atom behaviour so the pattern is smooth and in accordance with values predicted by the independent atomic model (IAM) and the mixture rule.

The phase relationship between the inelastically scattered X-rays is essentially random, so no interference effects are evident. Hence the incoherent scattering profiles for molecules are the same as those predicted by the IAM.

The present study considers scattering by water which is an important constituent of all biological materials. Differential scattering cross-sections for water are presented in Fig. 5, evaluated using Eqs. (5) and (6),

the scattering factors of Hubbell et al. (1975) and molecular form factors of Peplow and Verghese (1998). Note that for small θ , the coherent differential scattering cross-sections are much larger than those for incoherent scattering at any angle. The total respective cross-sections are obtained by integrating over the solid angle $d\Omega = 2\pi \sin\theta d\theta$, arranged as an annulus with angular width $d\theta$, so the $\sin\theta$ weighting gives $\sigma_{\text{coh}} \leq \sigma_{\text{inc}}$.

2.3. Quantifying systematic errors due to forward scattering

The intensity of forward scattered photons can be estimated from the normalised scattering fraction (Barrett and Swindell, 1981),

$$\text{NSF}(\theta_{\text{cone}}) = \frac{\int_0^{\theta_{\text{cone}}} \left(\frac{d\sigma_{\text{sc}}}{d\Omega} \right) d\Omega}{\int_0^{\pi} \left(\frac{d\sigma_{\text{sc}}}{d\Omega} \right) d\Omega} \quad (7)$$

which represents fraction of scattered photons that are redirected into a forward cone with half angle θ_{cone} . Assuming a single scattering interaction and ignoring attenuation, the total intensity reaching the detector is given by

$$I_t + I_{\text{coh}} + I_{\text{inc}} = I_t [1 + f_{\text{coh}} \text{NSF}_{\text{coh}}(\theta_{\text{cone}}) + f_{\text{inc}} \text{NSF}_{\text{inc}}(\theta_{\text{cone}})], \quad (8)$$

where f_{coh} and f_{inc} denote the fractional contribution to the total cross-section from the respective scattering

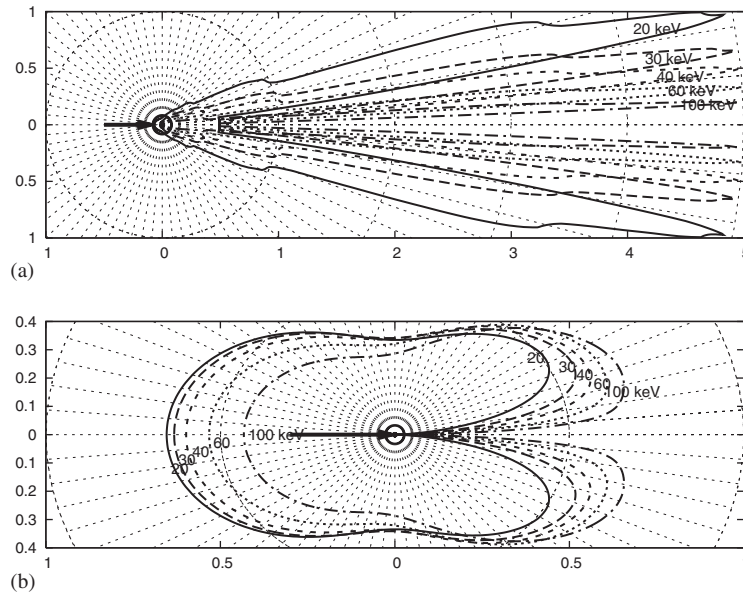


Fig. 5. Polar representation of (a) coherent and (b) incoherent differential scattering cross-sections (barn/molecule) for water.

processes as illustrated in Fig. 2. The ray-sum error in Eq. (3) is determined by the SPR which is obtained by rearranging the previous expression, i.e.,

$$\text{SPR} = \frac{I_{\text{coh}} + I_{\text{inc}}}{I_{\text{t}}} = f_{\text{coh}} \text{NSF}_{\text{coh}}(\theta_{\text{cone}}) + f_{\text{inc}} \text{NSF}_{\text{inc}}(\theta_{\text{cone}}). \quad (9)$$

For a pencil beam irradiation geometry, Monte Carlo studies have shown that forward scattered radiation is almost exclusively single coherent scatter for energies below 100 keV or single incoherent scatter at higher energies (see e.g., Neitzel et al., 1985; Jaffray et al., 1994). For a homogeneous sample and for small scattering angles, the primary and scattered beams traverse similar path lengths through the sample. These differ by the factor $1/\cos\theta - 1$, which is 0.4–1.5% at 5–10°. Therefore, it is reasonable to neglect multiple scattering interactions and attenuation of the scattered radiation.

2.4. Calculation methods

The SPR was evaluated for both scattering processes as a function of the scatter acceptance angle, photon energy and sample composition. Differential scattering cross-sections were evaluated using Eqs. (4) and (5) for the angular range $0 \leq \theta \leq \pi$; this exhibited varying degrees of granularity and was very fine at angles below 10°. Atomic form factors (Hubbell and Øverbø, 1979) and incoherent scattering factors (Hubbell et al., 1975) tabulated at 50 momentum transfer points,

$0 \leq x \leq 28 \text{ \AA}^{-1}$, were interpolated using a rational function algorithm with five degrees of freedom (Press et al., 1992) onto a finer grid according to the desired energy and scattering angle. The normalised scatter fraction given by Eq. (7) was evaluated using the trapezoidal rule, then an iterative search was conducted to find the scatter acceptance angle for a given ray-sum error. A systematic error of 0.5–1.0% in evaluating μ , was deemed to be an acceptable compromise in the trade off between minimising the SPR whilst still maintaining sufficient transmitted intensity.

3. Results

The SPR for coherent scattering was evaluated using Eqs. (4) and (9), and tabulated atomic form factors (Hubbell and Øverbø, 1979). Results are presented in Fig. 6 for the energy range 5–1000 keV where this interaction is of some importance. The results for forward direction incoherent scattering are presented in Fig. 7 for a broader range of energies extending to 100 MeV. These were evaluated using Eqs. (5) and (9) and tabulated incoherent scattering functions (Hubbell et al., 1975). Fig. 8 gives the scatter acceptance angle when both scattering processes are considered together. The results for scattering by water are presented in Fig. 9, for both processes. This data compares three scatter distributions: (a) the IAM, using tabulated $F(x, Z)$ and $S(x, Z)$, (b) the IAM and free electron incoherent scatter (i.e., $S(x, Z) = 1$), and (c) a more

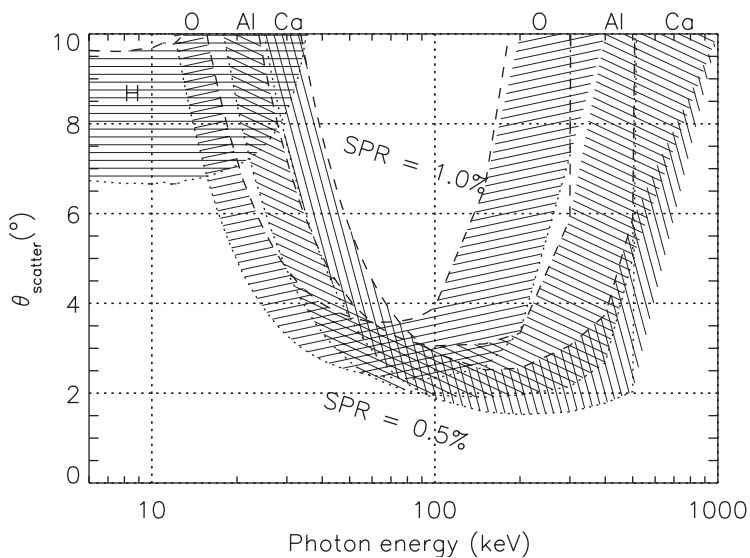


Fig. 6. Scatter acceptance angles where SPR = 0.5–1.0%, for coherent scattering.

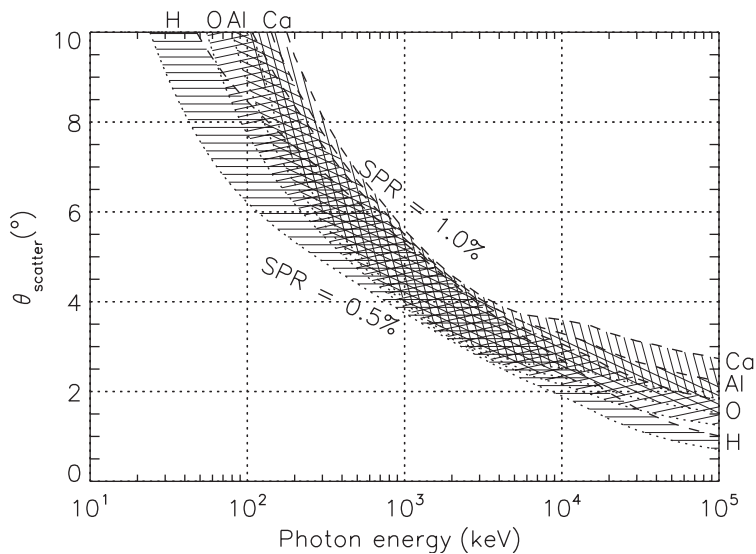


Fig. 7. Scatter acceptance angles where SPR = 0.5–1.0%, for incoherent scattering.

realistic scenario based upon published molecular form factors (Peplow and Verghese, 1998) and tabulated $S(x, Z)$.

4. Discussion

The probability for coherent scattering interactions for low Z elements (excluding hydrogen) is approximately 10% at energies 10–100 keV (see Fig. 2(a)). Half

angles that give an acceptable SPR are strongly dependant upon both photon energy and sample composition (see Fig. 6). For energies below 20 keV, where the angular distribution of coherently scattered radiation is relatively broad (see Fig. 3), the scatter acceptance angle exceeds 6°. At energies above 20 keV, the coherent scatter angular distributions contract and a tolerable scatter acceptance angle at 60 keV is approximately 3°. The narrowest scatter acceptance angle is about 2° at 80 keV for oxygen, 100 keV for aluminium

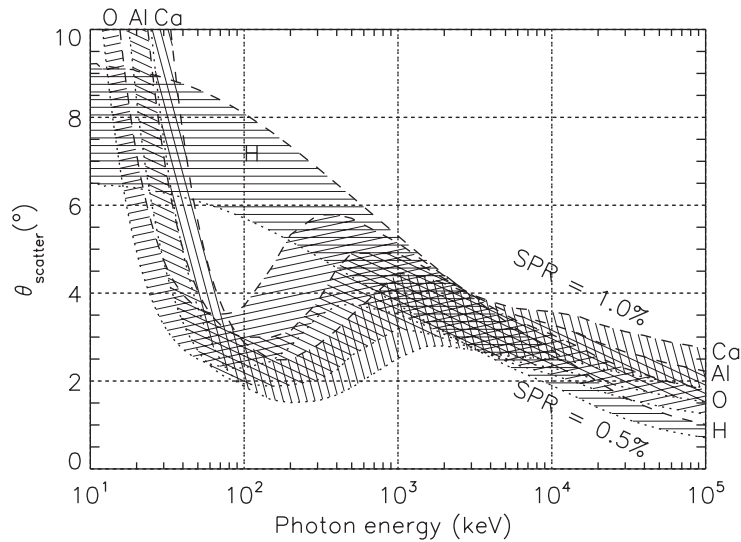


Fig. 8. Scatter acceptance angles where $\text{SPR} = 0.5\text{--}1.0\%$ for both processes.

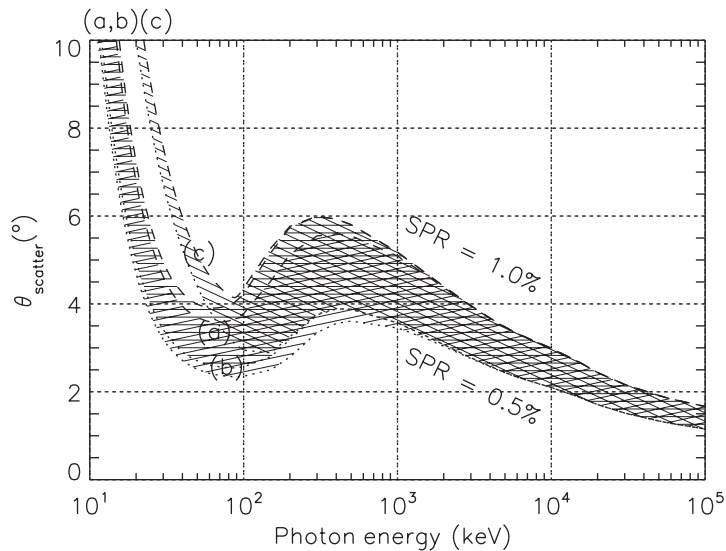


Fig. 9. Scatter acceptance angles where $\text{SPR} = 0.5\text{--}1.0\%$ for water and both scattering processes. Calculations utilise (a) the IAM ($F_{\text{IAM}}(x), S(x)$) (b) the IAM and Compton scattering ($F_{\text{IAM}}(x), S = 1$) and (c) molecular scattering ($F_{\text{mol}}(x), S(x)$).

and 200 keV for calcium. At higher energies, this interaction is of lesser importance (see Fig. 2(a)), and the requirement for a narrow scatter acceptance angle can be relaxed.

As the photon energy increases, incoherent scattering becomes the dominant interaction process (see Fig. 2(b)), with an angular distribution that becomes peaked in the forward direction at mega voltage energies. This trend is evidenced in Fig. 7 where the scatter acceptance angle for the desired SPR decreases with increasing photon energy. At mega voltage

energies, the half angle for 0.5% SPR should not exceed $3.7\text{--}1.8^\circ$ at $1\text{--}10$ MeV. At energies above 10 MeV and for all materials except those containing hydrogen, the scatter acceptance angle becomes wider. This can be attributed to pair production becoming important for higher Z elements whilst triplet production is of some significance for lower Z elements.

When both scattering processes are considered together (see Fig. 8), the scatter acceptance angles at mega voltages are similar to those of incoherent scattering alone. The acceptance angle increases at lower energies

reaching a maximum value of $6\text{--}8^\circ$ near 100 keV, then falls to $2\text{--}4^\circ$ at 30–60 keV, and again increases at lower energies. This complicated behaviour can be attributed to the energy dependence for each process and the resultant angular pattern of scattered radiation.

Fig. 9 compares results for scattering by water based upon (a) the IAM, (b) the IAM with Compton scattering (i.e., free electron behaviour) and (c) molecular scattering. The scatter acceptance angle is relatively wide at low energies, where the coherent scatter distribution is broad, becoming narrower at high energies as the coherent distribution contracts and the incoherent scatter distribution becomes forward peaked. The choice of atomic model is also important. At energies below 100 keV, molecular scattering factors suppress forward scattering (compare Figs. 3(a) and 5(a)) so the acceptance angle for molecular scattering is wider than for the IAM data (Figs. 9(c) and (a), respectively). When incoherent scattering factors are neglected (Fig. 9(b) whereby $S(x) = 1$) forward direction incoherent scatter is no longer suppressed and the scatter acceptance angle is even narrower at low and very high energies.

5. Conclusions

The aim of this investigation was to prescribe the maximum angular width of a “narrow” beam for accurate μ measurements. This angle was defined in Fig. 1 and allows to the detector record a cone of forward scattered radiation. Our criteria for selecting this angle was based upon tolerating ray-sum errors of 0.5–1.0% due the detection of scattered radiation.

The angular distribution of incoherent scattered photons is given by the Klein-Nishina differential scattering cross-section modified by the incoherent scattering function, which suppresses forward direction scattering (see Fig. 4). In Fig. 7, the scatter acceptance angle for incoherent scattering by $1 \leq Z \leq 20$ exceeds 6° at low energies. At higher energies, the distribution becomes more forward peaked, and this angle decreases to $4\text{--}2^\circ$ at 1–10 MeV.

Although coherent scattering is generally of far lesser importance (see Fig. 2), the angular distribution is peaked in the forward direction, and this places a more stringent requirement on the scatter acceptance angle. The coherent scattering acceptance angles presented in Figs. 6 are a function of photon energy and sample composition. At energies 30–100 keV and for $Z \leq 20$, this angle should not exceed about 3° . Fig. 8 considers both scattering interactions, whereby the scatter acceptance angle has a narrow minimum at diagnostic X-ray energies, and should not exceed $2\text{--}4^\circ$ at 30–60 keV.

When molecular scattering factors are taken into account, the coherent scatter distribution is suppressed in the forward direction (see Fig. 5), leading to more

generous scatter acceptance angles. For water, this should not exceed about 3° at 100 keV, 5° at 50 keV and 10° at 20 keV.

The results presented in this report can be used to prescribe the angular width for narrow beam monoenergetic μ measurements at photon energies 5 keV to 125 MeV. The narrowest beams are required at diagnostic X-ray energies, approximately 2° at 50–150 keV depending upon the sample composition, and at very high mega voltage energies, where the incoherent scatter distribution is confined to the extreme forward direction. Our predictions at lower energies are based upon the IAM which is an approximation. In reality, molecular interference effects suppress coherent scattering in the forward direction, so the scatter acceptance angle is slightly wider. Further work is required to explore this issue, as molecular scattering factors become available for other materials.

References

- Barrett, H.H., Swindell, W., 1981. Radiological Imaging: The Theory of Image Formation, Detection and Processing. New York Academic, New York, pp. 562–567.
- Boone, J.M., Chavez, A.E., 1996. Comparison of X-ray cross-sections for diagnostic and therapeutic medical physics. Med. Phys. 23, 1997–2005.
- Creagh, D.C., Hubbell, J.H., 1987. Problems with the measurement of X-ray attenuation coefficients. I: Silicon. Report on the international union of crystallography X-ray attenuation project. Acta Cryst. A 43, 102–112.
- Creagh, D.C., Hubbell, J.H., 1990. Problems associated with the measurement of X-ray attenuation coefficients. II: Carbon. Report on the international union of crystallography X-ray attenuation project. Acta Cryst. A 46, 402–408.
- Cullen, D.E., Chen, M.H., Hubbell, J.H., et al., 1989. Tables and graphs of photon interaction cross-sections from 10 eV to 100 GeV derived from the LLNL evaluated photon data library (EPDL). National Technical Information Service, US Department of Commerce, Springfield, VA.
- Davison, C.M., Evans, R.D., 1952. Gamma ray absorption measurements. Rev. Mod. Phys. 24, 79–107.
- Harding, G., Schreiber, B., 1999. Coherent scatter imaging and its applications in biomedical sciences and industry. Rad. Phys. Chem. 56, 229–245.
- Hubbell, J.H., Øverbø, I., 1979. Relativistic atomic form factors and photon coherent scattering cross-sections. J. Phys. Chem. Ref. Data 8, 69–105.
- Hubbell, J.H., Viegle, Wm.J., Briggs, E.A., Brown, R.T., Cromer, D.T., Howerton, R.J., 1975. Atomic form factors, incoherent scattering functions and photon cross-sections. J. Phys. Chem. Ref. Data 3, 417–538.
- Jaffray, D.A., Battista, J.J., Fenster, A., Munro, P., 1994. X-ray scatter in mega-voltage transmission radiography: physical characteristics and influence on image quality. Med. Phys. 21, 45–60.
- Johns, P.C., Yaffe, M.J., 1983. Coherent scatter in diagnostic radiology. Med. Phys. 10, 40–50.

- Kozanetzky, J., Knoerr, B., Harding, G., Neitzel, U., 1987. X-ray diffraction measurements of some plastic materials and body tissues. *Med. Phys.* 14, 526–532.
- Morin, L.R., Berroir, A., 1983. Calculation of X-ray single scattering in diagnostic radiology. *Phys. Med. Biol.* 28, 789–797.
- Neitzel, U., Kosanetzky, J., Harding, G., 1985. Coherent scattering in radiographic imaging: a Monte Carlo simulation study. *Phys. Med. Biol.* 30, 1289–1296.
- Peplow, D.C., Verghese, K., 1998. Measured molecular coherent scattering form factors of animal tissues, plastics and human breast tissue. *Phys. Med. Biol.* 43, 2431–2452.
- Perrin, F.H., 1948. Whose absorption law? *Opt. Soc. Am.* 38, 72–74.
- Press, W.H., Teukolsky, S.A., Vetterling, W.T., Flannery, B.P., 1992. *Numerical Recipes in C. The Art of Scientific Computing*, 2nd ed. Cambridge University Press, Cambridge, pp. 105–164.